Implications of Both Statistical Equilibrium and Global Warming Simulations with CCSM3. Part II: On the Multidecadal Variability in the North Atlantic Basin

MARC D'ORGEVILLE AND W. RICHARD PELTIER

Department of Physics, University of Toronto, Toronto, Ontario, Canada

(Manuscript received 7 August 2008, in final form 30 April 2009)

ABSTRACT

The nature of the multidecadal variability in the North Atlantic basin is investigated through detailed analysis of multicentury integrations performed using the low-resolution version of the Community Climate System Model, version 3 (CCSM3), a modern atmosphere–ocean coupled general circulation model. Specifically, the results of control simulations under both preindustrial and present-day perpetual seasonal cycle conditions are compared to each other and also to the results of five simulations with increasing CO_2 concentration scenarios.

In the absence of greenhouse gas–induced warming, the meridional overturning circulation (MOC) variability is shown to be dependent on the details of the simulation. In the present-day control simulation, the MOC is characterized by a broad spectrum of low frequencies, whereas, in preindustrial control simulations, MOC variability is characterized either by a well-defined periodicity of 60 yr or by a broad spectrum of low frequencies. In all the control simulations, the MOC appears to respond with a delay of 10 yr to synchronous temperature and salinity anomalies in the deep water formation sites located in the subpolar gyre, but salinity dominates the density anomalies. The explanation of the modeled MOC periodicity is therefore sought in the creation of these density anomalies. The influence of increased sea ice coverage under cold/preindustrial conditions is shown to modify the salinity variability, but it is not a sufficient condition for the support of the MOC periodicity. Instead, its source appears to be a modified subpolar gyre circulation resulting from interaction with the bottom bathymetry, which is able to sustain strong coupling between the horizontal and overturning circulations.

Based on the global warming analyses, for the simulations initialized from the cold/preindustrial statistical equilibrium run, the North Atlantic variability continues to be dominated by strong coupling between the horizontal and overturning circulations if the imposed forcing is weak. More generally, the delayed response of the MOC to surface density anomalies in the deep water formation regions is preserved under weak forcing.

1. Introduction

In the North Atlantic basin, a coherent basin-wide pattern of variability in sea surface temperatures (SSTs) has been identified with a period of 60–80 yr (Schlesinger and Ramankutty 1994). With an amplitude on the order of ½°C, this Atlantic multidecadal oscillation (AMO) has been linked to changes in North American rainfall and river flow, to Sahel drought, to ENSO intensity, to the modulation of hurricanes, and to North Pacific SST variability (Rowell et al. 1995; Goldenberg et al. 2001; Enfield et al. 2001; Rogers and Coleman 2003; Molinari and Mestas-Nuñez 2003; McCabe et al. 2004; Sutton and Hodson 2005; Dong et al. 2006; d'Orgeville and Peltier 2007; Zhang et al. 2007).

The instrumental record employed in the SST reconstructions on which the AMO index is based covers only the last 150 yr (Rayner et al. 2003; Smith and Reynolds 2004). The multidecadal time scale that appears to characterize the AMO can therefore be questioned on the basis of statistical significance. Paleoclimate proxy evidence, however, has been interpreted to suggest that an AMO with the same 60–80-yr period was also operative in previous centuries (Delworth and Mann 2000; Gray et al. 2004).

Given its finite amplitude, it is also recognized that the shift of the phase of the AMO from positive in the 40s to negative in the 70s has most probably contributed to a masking of the ongoing influence of global warming. Unsurprisingly, therefore, there is an ongoing debate as to what fraction of the AMO might be due to natural

Corresponding author address: Marc d'Orgeville, Climate Change Research Centre, Faculty of Science, UNSW, Sydney 2052, NSW, Australia.
E-mail: marcdo@unsw.edu.au

DOI: 10.1175/2009JCLI2775.1

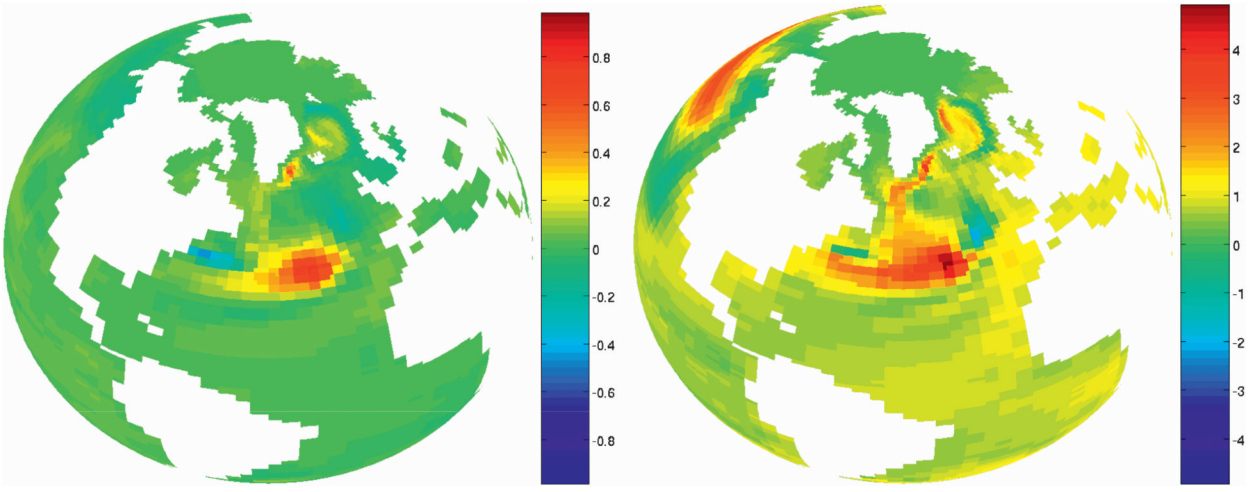

FIG. 1. Comparison for the twentieth-century simulation of (left) the first EOF of SST in the North Atlantic and (right) the warming SST pattern (difference between the periods 1870–79 and 1990–99). Color bars (°C).

variability as opposed to being directly forced by the secular influence of global warming (Trenberth and Shea 2006; Zhang et al. 2007). A deeper understanding of the mechanisms that underlie the low-frequency variability in the North Atlantic is therefore required, not only to enable its use in the context of climate predictability, but also to enable the intrinsic variability of the climate system to be disentangled from the anthropogenically forced global warming.

The available observations, both instrumental records as well as climate proxies, are too sparse to serve as a means to identify the mechanisms that lead to the occurrence of such low-frequency climate variability in the North Atlantic basin. We are therefore obliged to resort to the analysis of model simulations. From this perspective, it has been clear even on the basis of the earliest applications of global coupled ocean–atmosphere general circulation models based on long-time-scale simulations, that the SST variability in the North Atlantic was linked to the variability of the meridional overturning circulation (MOC; Delworth et al. 1993).

In global warming experiments, on the other hand, it has been previously demonstrated that the amplitude of the reduction of the MOC in response to greenhouse gas–induced warming of the lowest atmosphere is a function of the mean climate from which warming ensues, essentially because of the impact upon sea ice coverage in the deep water formation (DWF) region of the Labrador Sea (Weaver et al. 2007). However, that study was based on a model of intermediate complexity in which significant low-frequency North Atlantic (MOC) variability did not exist. In d'Orgeville and Peltier (2009, hereafter Part I), it was demonstrated that the North Pacific decadal variability was significantly influenced by strong greenhouse gas warming. In the North Atlantic also, as in the North Pacific, the spatial structure of the warming in SST displays a pattern similar to that of the dominant mode of SST variability (shown, e.g., in the twentieth-century simulation to be discussed herein; Fig. 1). This suggests that greenhouse gas warming might also be expected to influence the multidecadal variability of the North Atlantic.

Based on analyses of the same multicentury integrations described in Part I, all performed using the National Center for Atmospheric Research (NCAR) Community Climate System Model, version 3 (CCSM3) coupled atmosphere–ocean general circulation model, the first goal of this paper is to demonstrate that global warming can indeed exert significant influence on North Atlantic multidecadal variability of the MOC. However, prior to the discussion of the results obtained in appropriate warming experiments, it will be necessary to first characterize the nature of MOC variability in our control simulations with respect to its current understanding in the literature.

The prevalent idea supporting the notion of a linkage between SST and MOC variability is based on the recognition of a feedback loop that operates in the North Atlantic domain, which acts as follows: an SST anomaly, through its influence on density, may modulate the intensity of deep water formation and therefore the strength of the MOC; the variability of MOC intensity in turn may modulate the northward heat transport and therefore the amplitude of the SST anomaly. To explain the apparent oscillatory character of both the MOC and SST, two further ingredients (salinity and atmospheric variability) have been invoked to refine this basic concept. The role of salinity and atmospheric forcing in sustaining such oscillatory behavior has been extensively

studied in the context of uncoupled ocean-only general circulation models (see, e.g., Weaver and Sarachik 1991; Winton and Sarachik 1993). In the present paper, our focus will be on the results delivered by a fully coupled model.

A sea surface salinity (SSS) anomaly in the North Atlantic, through its influence on density, may also of course modulate the deep water formation process and SSS anomalies seem to play an important role in all of the descriptions of previously modeled MOC variability. The key mechanism initially invoked to support the existence of such oscillatory behavior was related to a time delay between the development of SST and SSS anomalies over the North Atlantic (Delworth et al. 1993), but this notion has recently been challenged on the basis of the results obtained with higher-resolution models (Danabasoglu 2008, hereafter D08). In the original scenario, the adjustment of the oceanic gyres to large-scale density anomalies was suggested to either decelerate or accelerate the advection of the anomalies around the basin (Delworth et al. 1993). The transport of freshwater and sea ice from the Arctic Ocean was also seen to play some role in the modulation of MOC variability (Delworth et al. 1997).

Atmospheric variability has also been shown to be linked to this mode of low-frequency behavior, mainly through modulation by the North Atlantic Oscillation (NAO; Dong and Sutton 2005; Dai et al. 2005). There is also an ongoing issue as to whether the low-frequency variability in the North Atlantic might arise because of a coupled ocean–atmosphere mode of internal variability (Timmermann et al. 1998; Weaver and Valcke 1998) or from a damped ocean-only mode that is continuously excited by atmospheric stochastic forcing (Delworth and Greatbatch 2000; Dong and Sutton 2005).

From a mechanistic point of view, it therefore seems that all such explanations of MOC variability have been based on a specific subset of plausible physical interactions. These interactions are of course represented in any model, but depending on the model one or the other set may be more or less dominant, leading to either slightly or significantly different modeled North Atlantic variability. One specific consequence of this seems to be that different models deliver significantly different time scales of MOC variability that vary from 25 to 100 yr [e.g., Dong and Sutton (2005) and Knight et al. (2005) for the shorter and longer time scales, respectively].

In this study, the nature of the multidecadal variability in the North Atlantic Ocean is investigated in multicentury integrations performed using the NCAR–CCSM3 model. For this specific model, it has already been demonstrated that the intensity of MOC variability is resolution dependent in control simulations and also that it might be significantly reduced as a consequence of transient climate forcing because of continuous increase of the atmospheric CO_2 concentration (Bryan et al. 2006). In the analysis presented in this paper, control simulations under both preindustrial and present-day perpetual seasonal cycle conditions will be compared to each other and also to the results of five simulations with increasing CO_2 concentration scenarios. The same model with the same resolution is used in all of the simulations to be reported in order to remove discrepancies that could otherwise be attributed to the use of different models or different resolution-dependent subgrid-scale parameterizations.

The analyses presented will be based primarily on comparison of the results obtained from two control simulations that exhibit characteristically different MOC variability. Specifically, a periodic multidecadal mode of variability with a well-defined time scale of 60 yr is found to dominate the variability of all variables during part of the preindustrial control simulation. This feature, absent in the present-day control simulation, is reminiscent of the 20-yr periodic mode found in a simulation using the highest-resolution version (T85x1) of the same CCSM3 model (D08).

In the analysis of our control simulations, we will first attempt to determine which of the major differences in the mean climate between the two control simulations could explain the differences in multidecadal variability. More specifically, (i) how does the variation of mean sea ice coverage impact SSS and MOC variability? (ii) How do the different barotropic circulations influence the MOC variability? (iii) Finally, what is the origin of the quasi periodicity of the MOC in a portion of the preindustrial control simulation, and what are the roles of SST, SSS, and barotropic circulations? In so far as it is possible, we will compare our results with those of D08 obtained with a higher-resolution simulation. Answers to these questions will aid in the investigation of the extent to which the influence of global warming might be expected to impact modeled MOC variability.

It is important to note that compared to observations the CCSM3 ocean component of the coupled model has its largest mean biases in the North Atlantic basin, which is of interest to us here (Large and Danabasoglu 2006; Yeager et al. 2006); the Gulf Stream is predicted by the model to be excessively zonal and the sea ice coverage overly extensive, errors that are both expected to be responsible for the significant SST and SSS biases compared to observations. Although direct comparison of our results with observations will therefore not be immune to criticism as a consequence of these mean state biases, it has still proven possible to gain valuable information on the processes responsible for low-frequency

TABLE 1. List of simulations with run characteristics.

Run name	Forcing	Duration	Analysis on	Initial yr	From run
1870-control	1870 annual cycle	1100	2270–2569	1870	Start-up
1870-control 2	1870 annual cycle	1100	2670–2969	1870	Start-up
1870–0.5%	Increase of 0.5% CO_2 yr^{-1}	200	2370–2569	2370	1870-control
1870–1.0%	Increase of 1.0% CO_2 yr^{-1}	200	2370–2569	2370	1870-control
1870–2000	Twentieth century	130	1870–1999	2370	1870-control
1990-control	1990 annual cycle	705	400–700	1	Start-up
1990–0.5%	Increase of 0.5% CO_2 yr^{-1}	200	506–705	506	1990-control
1990–1.0%	Increase of 1.0% CO_2 yr^{-1}	200	506–705	506	1990-control

variability through the comparison of a set of appropriately designed simulations.

This article is organized as follows: in section 2, the numerical simulations to be analyzed are described, together with the spatial and time filtering of the outputs to be employed and the technical aspects of the analyses to be performed. Sections 3–6 present our detailed analyses of the modeled North Atlantic variability in the control simulations. The different temporal characteristics of the multidecadal variability of the MOC are introduced in section 3. Section 4 provides an overview of the differences in mean state between the control simulations that we have employed. Section 5 describes the considerably different surface variability delivered by two simulations. Section 6 compares the multidecadal variability of North Atlantic surface variables with the MOC variability in order to clarify the cause of the differences. The effect of global warming on North Atlantic natural variability is examined subsequently in section 7. Section 8 summarizes our findings and provides tentative answers to the specific questions upon which we have elected to focus.

2. Numerical experiments and analysis procedures

The numerical experiments and the diagnostic analyses are essentially the same as those in Part I. The descriptions are repeated here so that this part of the study is self contained. The differences between this section and section 2 of Part I are in italics to make the overlaps explicit.

a. The coupled atmosphere–ocean climate model

The model employed in this study is the CCSM3. The model has four interacting components—atmosphere, ocean, sea ice, and land surface—linked via a flux coupler. All of the simulations discussed in the following have been performed at T31 resolution for the atmospheric component (26 vertical levels and 3.75° horizontal resolution) and with a grid termed gx3v5 for the oceanic component (25 vertical levels, 3.6° resolution in the zonal direction and variable in the meridional direction with approximately 0.6° resolution near the equator). *In gx3v5, because the north pole of the grid is located over Greenland, the deep water formation regions located in the Labrador and in the Greenland, Iceland, and Norwegian (GIN) Seas have grid cells with an aspect ratio close to 1 and a typical-length scale less than 150 km.* A detailed description of the model can be found in Collins et al. (2006), and a detailed description of this specific resolution can be found in Yeager et al. (2006).

The simulations consist primarily of two ''control'' computations under perpetual annual cycle forcing corresponding to 1870 and 1990 epoch climate conditions, with durations of 1100 and 700 yr, respectively. The period of 400–700 yr of these 1870 and 1990 runs, to be referred to as 1870-control and 1990-control, respectively, are employed as the basis for the analyses reported in sections 3–6. *The period 800–1100 yr of the 1870 run, to be referred to as 1870-control 2, is also discussed.*

The two spinup runs have been further employed to provide two sets of initial conditions (at 500 yr) for a series of global warming simulations. From each spinup run, two 200-yr simulations forced by a constant rate of increase of 0.5% and 1% in CO_2 concentration per year have been branched off, with all other parameters kept fixed to those employed in the corresponding control run. A complete simulation of twentieth-century warming has also been performed from 1870 to 2000 as a continuation of the 1870 statistical equilibrium run with all climatic parameters evolving based on reconstructions described in Meehl et al. (2006): greenhouse gas concentrations, solar and volcanic forcing, sulfate aerosols, and ozone. The results obtained from these five warming simulations are described in section 7.

The reference names and properties of each of the eight simulations are summarized in Table 1.

b. Filtering procedures and diagnostic analyses

Because this study focuses on decadal to multidecadal time-scale variability, all the diagnostics presented will be based on low-pass filtered annual anomalies. These anomalies have been created by using a three-step diagnostic procedure: first, annual averages are computed from the monthly output; next, the mean and linear

trends are removed to produce anomaly fields; and finally, a low-pass filter based on a *20-yr* width Hanning window is applied to all time series.[1]

Classical empirical orthogonal function (EOF) analyses, with area-weighted time series, have been conducted on different variables for the *North Atlantic (NA) region defined as extending from 20° to 65°N and from 100°W to 0°E*. In the following, principal components (PCs) correspond to the time series of the evolution of the amplitude of each of the different EOFs, whereas the spatial pattern of the EOF is plotted over the entire North Atlantic basin after a regression at every grid point on its corresponding PC. The PCs are normalized by their standard deviation and are therefore unit variance time series. Consequently, the EOF spatial patterns have the dimension of the corresponding analyzed variable and their amplitude is relative to one standard deviation of their corresponding PCs.

Statistical significance of all the regression/correlation coefficients is assessed with a two-tailed Student's *t* test, taking into account effective degrees of freedom following Bretherton et al. (1999).

Power spectrum analyses based on a single periodogram are employed *on unfiltered annual anomaly time series* or on ''associated time series'' obtained by projecting raw (unfiltered) data onto the EOF spatial patterns, to ensure that time filters do not create artificial peaks (Saravanan and McWilliams 1997). The confidence levels, shown in all related plots are based on reference red-noise spectra with the same total variance and the same lag-1 autocorrelations as the analyzed time series (Mann and Lees 1996).

Fluxes are computed across the ocean surface from the atmosphere or the ice components to the ocean component, with a positive flux representing a gain by the ocean. Heat flux (HFLX) is the sum of all fluxes to the ocean (shortwave, longwave, latent, sensible, and sea ice melting/formation). Freshwater flux (FWFX) is also taken to be the sum of all fluxes to the ocean (evaporation, precipitation, runoff, sea ice melting/formation). Note that stress from the sea ice is included in the wind stress curl (WSC).

3. MOC variability in the control simulations

The MOC index is defined as the maximum of the meridional overturning streamfunction averaged over the latitudinal band 25°–35°N. Its time evolution is displayed in Fig. 2 for the two computations under 1870 and 1990 perpetual seasonal cycle conditions. For both simulations, the MOC index decreases from a value of approximately 19 Sv (1 Sv $\equiv 10^6$ m^3 s^{-1}) to approximately 14 Sv during the first 400 yr. The MOC index then stabilizes for the next 300 yr with averaged values of 13.4 and 14.1 Sv in 1870-control and 1990-control, respectively (for the range of time between the vertical dashed lines in Fig. 2).

In both control simulations, the average MOC has the same overall latitude–depth distribution, with a maximum located approximately at 30°N and at 1000-m depth (Fig. 2). Compared to the present-day simulation with CCSM3 at higher resolution (D08), the downwelling between 60° and 65°N is half as strong (Bryan et al. 2006). This weaker deep water formation north of 60°N can probably partly explain the shallower southward-flowing branch and the weaker average value of the MOC index (larger than 20 Sv in the T85x1 experiment of D08).

In Fig. 2, during the 300-yr period of the control simulations, the unfiltered MOC index has the same standard deviation, with a value of approximately 0.9 Sv in both simulations and negligible trends of 10^{-3} Sv yr^{-1} in 1870-control and -2.10^{-4} Sv yr^{-1} in 1990-control. However, the temporal behavior is obviously different between the two control simulations, with an apparent quasi-periodic oscillation in 1870-control and no apparent preferred time scale in 1990-control.

Figure 3 presents the first EOFs of the MOC for both control simulations. They explain 76% and 63% of the MOC variance in 1870-control and 1990-control, respectively. In both simulations, the EOF spatial structure is a monopole centered on the location of the maximum, but it extends to greater depth in 1870-control, which is reminiscent of the structure found by D08. The corresponding PCs have a correlation coefficient larger than 0.9 (99%) with the time-filtered MOC indices. Power spectra of the first EOF (Fig. 3) or of the MOC index (not shown) give exactly the same results in 1870-control, with one large and unique spectral peak significant at the 99% level. In contrast, in 1990-control, the same power spectra display multiple peaks with much lower amplitude, which are not significant at the 99% level (their significance can vary between 90% and 95%, depending on which of the first EOF associated time series or the MOC index is used). 1870-control presents, therefore, a well-defined period of approximately 60 yr, whereas 1990-control exhibits a spectrum of the MOC amplitude time series that is not statistically different from a red-noise hypothesis (at the 99% significance level).

The computation under 1870 perpetual seasonal cycle conditions was further extended for 400 additional years. Following the period denoted 1870-control, the

[1] The Hanning window is wider than in Part I because the focus here is on multidecadal time scales instead of decadal time scales.

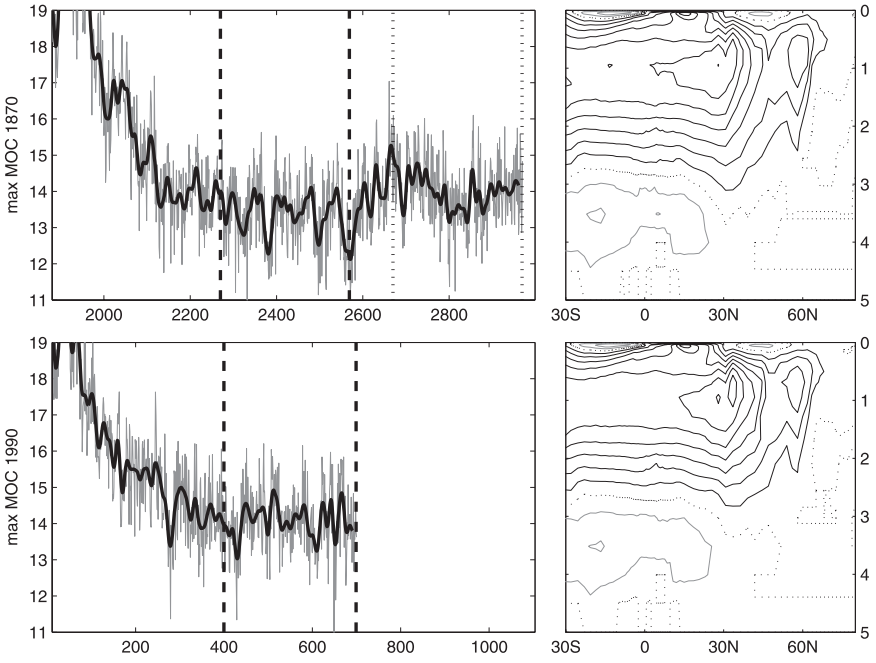

FIG. 2. (left) Time series of the MOC index in Sverdrups and (right) mean MOC for the two computations under perpetual annual cycle forcing corresponding to (top) 1870 and (bottom) 1990 epoch climate conditions. The thick lines in (left) are the low-pass filtered time series. Vertical dashed lines indicate the period 400–700 yr of 1870-control and 1990-control. Vertical dotted lines indicate the period 800–1100 yr, 1870-control 2. In (right), the isolines are every 2 Sv; the zero line is dotted; positive and negative values are in black and gray, respectively; and the depth (km).

MOC index exhibits a clear transition before settling upon a new plateau in the last 300 yr of the computation (1870-control 2 for the range of time between the vertical dotted lines in Fig. 2), with an averaged value of 14 Sv, a standard deviation of approximately 0.9 Sv, a trend of amplitude 10^{-3} Sv yr^{-1}, and a power spectrum of the MOC index similar to 1990-control. The periodic behavior of the MOC in 1870-control appears therefore to be transient, as was also found to be the case in the higher-resolution version of the same CCSM3 model (D08).

4. Mean state in control simulations

This section provides an overview of the differences between the mean states of the two control simulations in order to explain the differences in surface variability (section 5) and MOC variability (section 6).

Because of a globally warmer climate, SSTs are globally warmer in 1990-control and there is reduced sea ice in the North Atlantic and the Arctic (Fig. 4). The increase of SST is accompanied by an increase of SSS, which is reminiscent of what is seen in the CO_2 doubling experiments but with the difference, in our case, that the mean amplitude of the MOC is not greatly affected (Bryan et al. 2006).

The second striking change between the two control simulations is seen in the barotropic stream function (BSF): the North Atlantic subpolar and subtropical gyres are stronger in 1990-control than in 1870-control (with differences of as much as 10 Sv), which leads to a stronger barotropic Gulf Stream, which is, however, not significantly displaced in latitude (Fig. 4). This difference is not due to the wind forcing because the wind stress curl in 1990-control is globally weaker in amplitude than in 1870-control (not shown).

The linear vorticity equation for a homogeneous ocean in the β-plane approximation can be written as

$$\beta V = \frac{\nabla \times \tau}{\rho_0} + F_{\mathrm{tb}}, \tag{1}$$

where V is the barotropic meridional transport; $\nabla \times \tau$ is the surface wind stress curl; ρ_0 is the mean ocean density; and F_{tb} is the effect of the variable bathymetry, which is directly proportional to the bottom pressure torque (Mellor et al. 1982; Greatbatch et al. 1991; Zhang and Vallis 2007). Comparison of the first two terms of the Sverdrup balance [Eq. (1); Fig. 5] indicates that processes other than the wind are playing an important role in setting up the two different mean barotropic circulations of the North Atlantic Ocean.

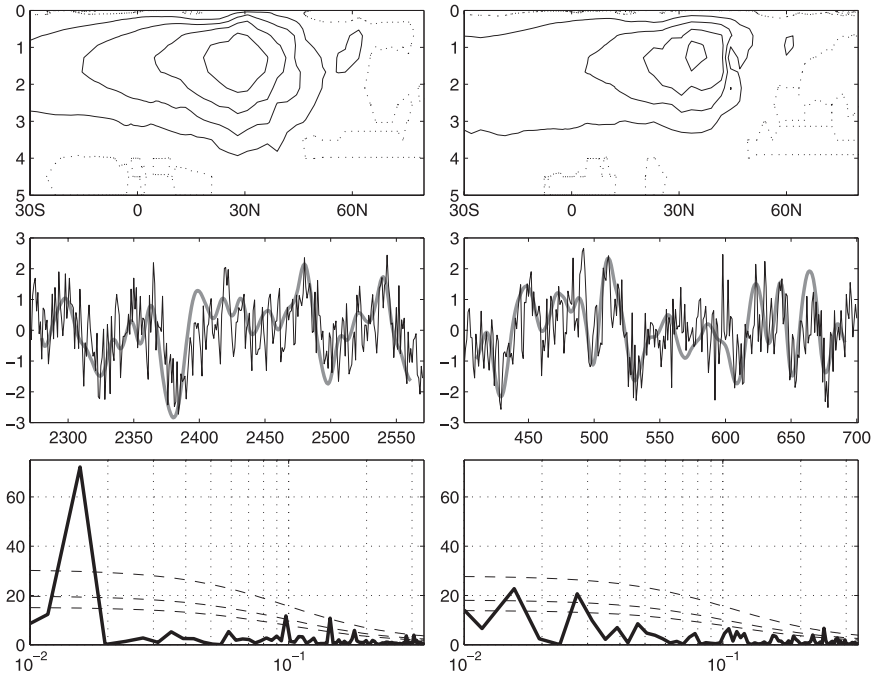

FIG. 3. (top) First EOF of the MOC (isolines every 0.1 Sv), (middle) corresponding PC (PC in gray and associated time series in black), and (bottom) power spectra of the associated time series (dashed lines correspond to the 90%, 95%, and 99% significant levels) for (left) 1870-control and (right) 1990-control. Frequency is in yr^{-1}.

The second term of the right-hand side of Eq. (1), F_{tb}, arises as a consequence of the variable bathymetry and implies that the vertically averaged flow is no longer decoupled from the rest of the motion when the fluid is stratified (see, e.g., Salmon 1998). The term F_{tb} can therefore be seen as representing the effect of a coupling between the baroclinic and the barotropic circulations resulting from the variable bathymetry. However, because F_{tb} requires the computation of a Jacobian whose diagnostic is very noisy on our oceanic grid, we choose to present an analysis based on the barotropic transport equations from which the above Sverdrup balance is derived; that is,

$$-fV = \frac{\tau^x}{\rho_0} - H\frac{\partial \mathrm{Pb}}{\partial x} - \frac{\partial \Phi}{\partial x},$$

$$fU = \frac{\tau^y}{\rho_0} - H\frac{\partial \mathrm{Pb}}{\partial y} - \frac{\partial \Phi}{\partial y},$$

where f is the Coriolis parameter; τ^x and τ^y are the wind stress; H is the variable depth; Pb is the (dynamical) bottom pressure; and Φ is the potential energy such that $\Phi = \int_{-H}^{0} bz\, dz$, where b is the negative of the buoyancy.

Following Mellor et al. (1982), we define the Ekman transport (V_e, U_e) and the transport resulting from the combination of the thermohaline circulation and the bottom velocity (V_{tb}, U_{tb}), such that

$$f(V_e, -U_e) = -\frac{(\tau^x, \tau^y)}{\rho_0},$$

$$f(V_{\mathrm{tb}}, -U_{\mathrm{tb}}) = H\nabla \mathrm{Pb} + \nabla\Phi.$$

The comparison of V, V_e, and V_{tb} (Fig. 6) shows unequivocally that the differences in barotropic transports between the two control simulations are primarily due to the effects of the thermohaline circulation and of the bottom velocity, an effect caused by the variable bathymetry.

To summarize, the two major differences in mean states of the North Atlantic basin between the two control simulations appear to be in the barotropic circulation (because of the interaction with the bottom bathymetry) and in the sea ice coverage (because of a warmer climate). In contrast, 1870-control 2 appears to have the same type of barotropic circulation as in 1990-control and the same sea ice distribution as in 1870-control (not shown).

5. Surface variability in the control simulations

This section presents an analysis in terms of EOFs of the surface variability in the two control simulations, highlighting their differences, as an aid in the explanation of the difference in MOC variability discussed in

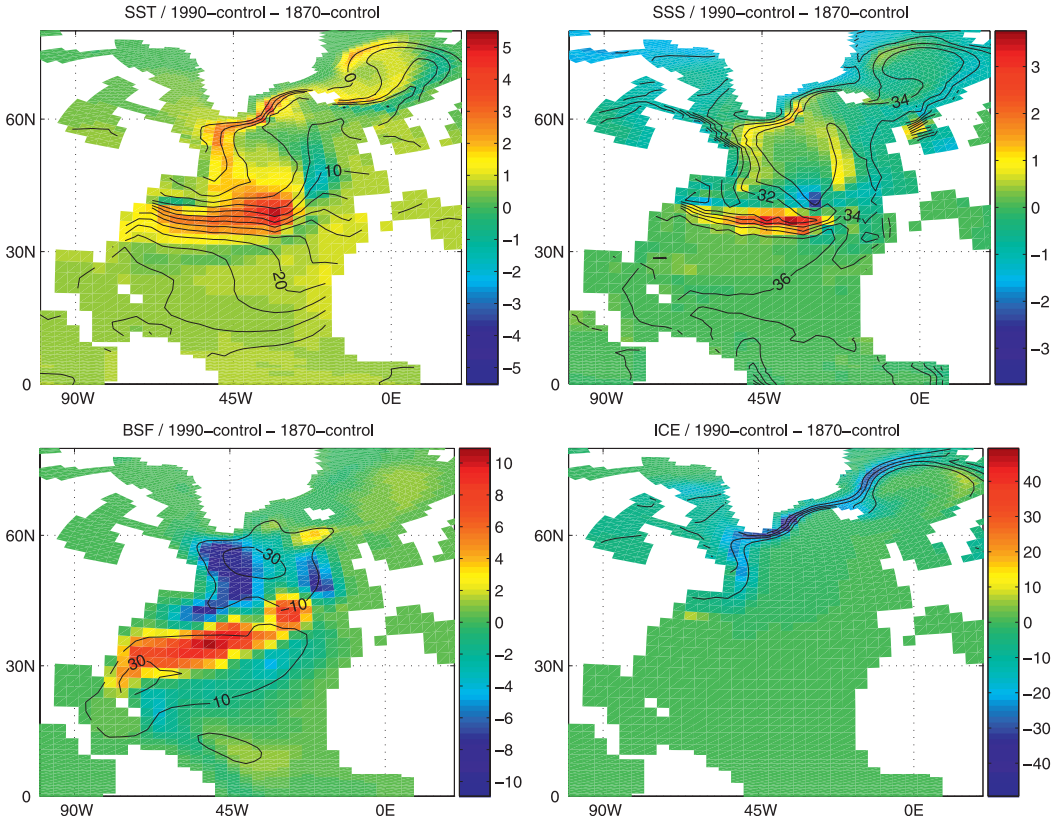

FIG. 4. Differences between the means in 1990-control and 1870-control (color) and the isolines of the mean fields from simulation 1870-control for (top left) SST, (top right) SSS, (bottom left) BSF, and (bottom right) sea ice coverage. The isolines are as follows: from 0° to 30° every 2° for SST, from 25 to 38 psu every 1 psu for SSS, from −30 to 30 Sv every 20 Sv for BSF, and from 20% to 80% every 20% for sea ice coverage.

section 6. The explained variances by the first two EOFs of each variable are detailed in Table 2.

a. SST and SSS variability

In both control simulations, the spatial patterns of the first EOFs of SST (Fig. 7) display a common dipole pattern between the subtropical gyre and subpolar gyre (SPG), with the largest extremum of amplitude over the latitudes occupied by the Gulf Stream. This structure is far from the classical monopole of the observed Atlantic multidecadal oscillation (Delworth and Mann 2000), but it has the same north–south orientation as the dipolar

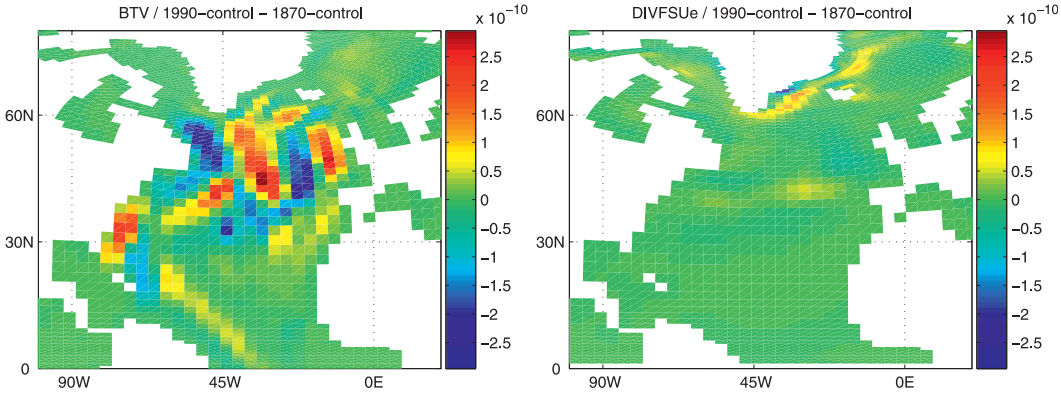

FIG. 5. As in Fig. 4, but for the first two terms of Eq. (1), (left) βV and (right) $\nabla \times \tau/\rho_0$ (m s^{-2}).

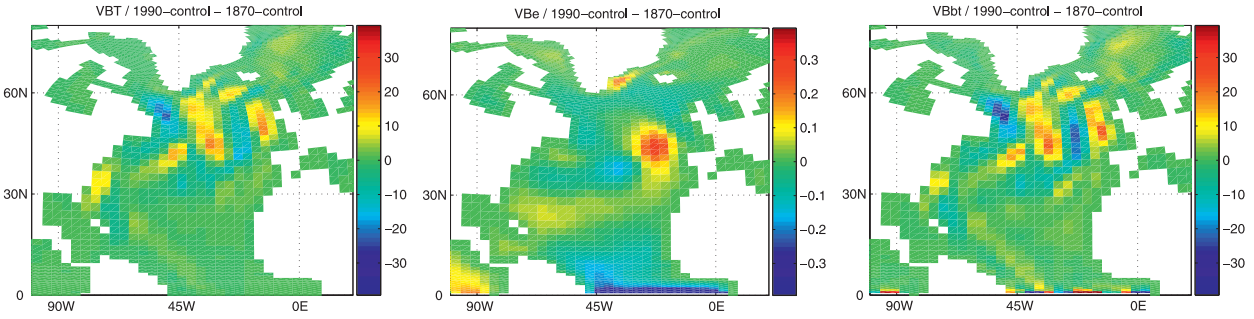

FIG. 6. As in Fig. 4, but for the meridional transport ($m^2\ s^{-1}$): (left) barotropic V, (middle) Ekman V_e, and (right) variable bathymetry V_{tb}. Note the difference of the amplitude of the Ekman color bar (middle).

SST mode observed by Deser and Blackmon (1993). This structure is also reminiscent of the SST tripole, which is linked to NAO variability with, however, a very weak signal in the center of the subtropical gyres (which is statistically significant only if the analysis is performed without time filtering).

In 1990-control, the first EOFs of SST and heat flux (Fig. 7) are closely related, with the SST leading the heat flux by 1 yr (time-lag correlation maximum of 0.9%–99%; Fig. 8). In 1870-control, the second EOF of heat flux (not shown), which explains almost as much variance as the first (see Table 2), presents the same spatial pattern as the first EOF of 1990-control and is also led by 2 yr by the first EOF of SST (time-lag correlation maximum of 0.9%–99%). This relationship corresponds to a loss (gain) of heat in the separation region of the Gulf Stream for a positive (negative) SST anomaly. This indicates that in both simulations the heat fluxes are not able to create the SST anomalies locally.

In both simulations, the first EOFs of SSS and freshwater flux are closely temporally related with the maximum of the time-lag correlation exceeding 0.8 (99%) when the flux leads by 1 or 2 yr (Fig. 8). In both simulations, the spatial patterns of the first EOFs of SSS have amplitude extrema along the latitude of the Gulf Stream (Fig. 7). In contrast, the first EOF of freshwater flux has extrema in the Labrador and Greenland Seas in 1870-control and in the separation region of the Gulf Stream in 1990-control, as was also the case for the first EOF of heat flux. This indicates that the East Greenland Current region and the Labrador Sea play a more significant role in the freshwater budget and in the heat budget of the North Atlantic in 1870-control.

Finally, there are two noticeable differences between the two simulations for the first EOFs of both SST and SSS (Fig. 7). First, the amplitude of the anomaly of opposite sign in the subpolar gyre is larger in 1870-control than in 1990-control. Second, the largest extremum is in the western part of the basin (in the separation region of the Gulf Stream) in 1990-control but in the eastern part of the basin (around 40°N, 30°W) in 1870-control.

b. *Barotropic circulation variability*

The first EOFs of wind stress curl are very similar in both simulations, whereas the first EOFs of the barotropic stream function (BSF) are strikingly different between the two simulations (Fig. 9): the amplitude extrema are two times larger in 1870-control than in 1990-control; the locations of the extrema are in the east of the basin around 40°N, 30°W in 1870-control and in the west of the basin in the separation region of the Gulf Stream in 1990-control; and the overall spatial pattern is characterized by large meanders around 40°N, 30°W in 1870-control, contrasting with the basin-wide aligned structure in 1990-control.

The amplitude of the maximum of time-lag correlation between the first EOFs of barotropic stream function and wind stress curl (reached when the wind is leading by 1 or 2 yr) is above 0.9 (99%) in 1990-control and smaller than 0.6 (99%) in 1870-control (Fig. 10). This indicates that barotropic circulation variability is a direct response to the wind variability in 1990-control, as can be expected on the basis of the Sverdrup relation but must have at least in part another origin in 1870-control.

In 1870-control, the presence of the meanders in the vicinity of the maximum height of the mid-Atlantic ridge

TABLE 2. Explained variance (%) by the first two EOFs of different variables in the North Atlantic for both control simulations.

Variable	1870-control	1990-control
SST	47–18	44–27
SSS	40–28	40–25
BSF	49–29	57–17
HFLX	36–26	44–13
FWFX	33–15	34–13
WSC	44–17	38–11
V_{tb}	65–15	36–23

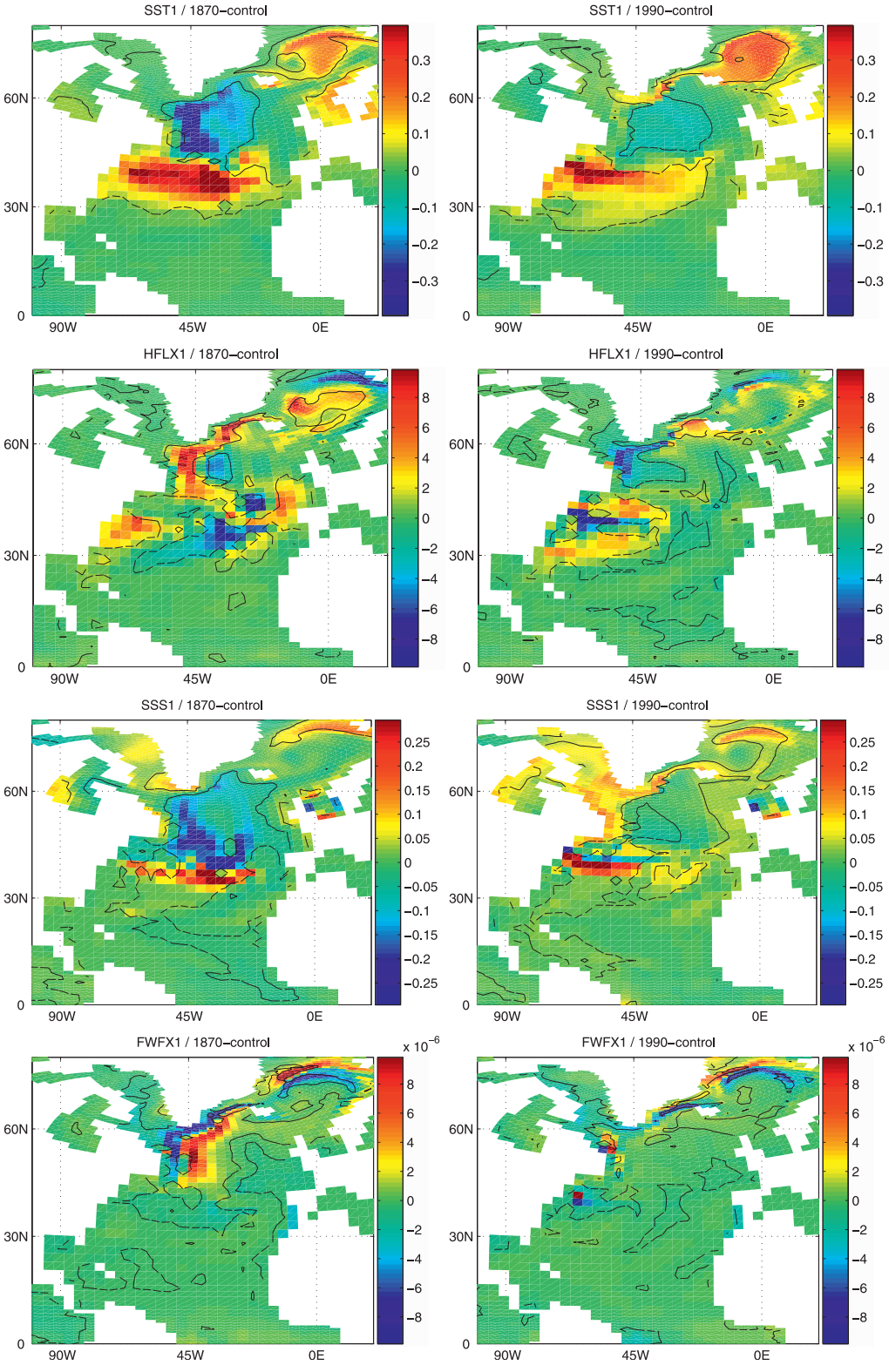

FIG. 7. EOF analyses of simulations (left) 1870-control and (right) 1990-control for first EOFs of (top)–(bottom) SST (°C), HFLX (W m^{-2}), SSS (psu), and FWFX (kg m^{-2} s^{-1}). Lines correspond to the limit of the 90% level of statistical significance.

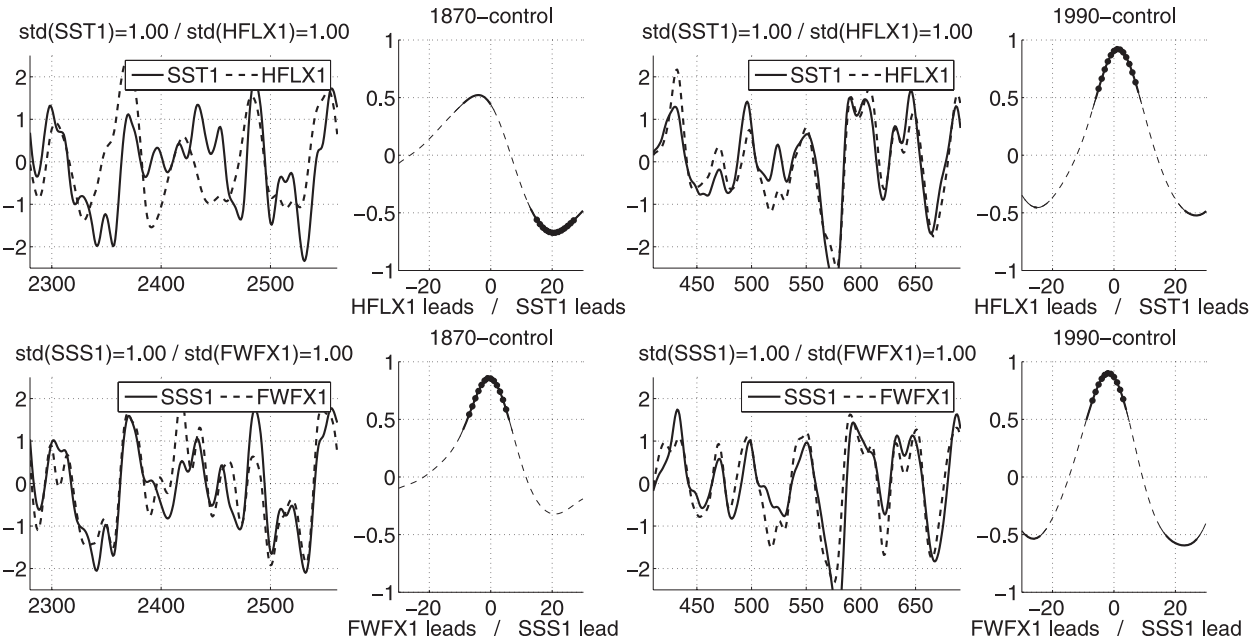

FIG. 8. Time-lag correlation (top) between first EOFs of SST and HFLX and (bottom) between first EOFs of SSS and FWFX for simulations (left) 1870-control and (right) 1990-control. Time series of the corresponding first PCs and their time-lag correlation function of the lag in years, with statistical significance at the 90% (solid line), 95% (thick solid line), and 99% (large dots) levels. State variables lead flux variables for positive lag.

located around 40°N, 30°W suggests that, in 1870-control, this other barotropic mode of variability could be due to an interaction of the current with the bottom bathymetry. This is further confirmed by the shape of the first EOF of V_{tb}, which displays a very localized east–west dipole corresponding to a maximum change of barotropic vorticity above this bathymetric feature (Fig. 9) and presents a maximum of time-lag correlation with the first EOF of BSF of almost 1 at lag 0 (Fig. 10). In contrast, in 1990-control, the first EOF of V_{tb} is trapped in the western boundary current and has a weaker maximum of time-lag correlation with the first EOF of BSF.

c. *Conclusions on the surface variability*

Taking into account that in 1870-control, as compared to 1990-control, more sea ice is present and the subpolar gyre is weaker (section 4), it seems evident that the difference of mean state between the two simulations is responsible for enabling these differences in surface variability. First, the increased sea ice coverage in the Labrador Sea and the East Greenland Current region appears to be responsible for the increased variability of heat and freshwater fluxes in these regions and subsequently the increased variability of SST and SSS in the subpolar gyre. Second, the weaker subpolar gyre appears to be able to support a different mode of variability than that arising solely from the wind, which is due to an interaction with the topography.

Analysis of the simulation 1870-control 2 (not shown) reveals the same patterns of variability as those of 1990-control, except for an increase of the amplitude of the SST and SSS anomalies in the subpolar gyre and for the freshwater flux extrema located in the Labrador Sea and the East Greenland Current region. Keeping in mind that the mean state of 1870-control 2 is similar to the mean state of 1990-control, except for an increase of the sea ice coverage because of a colder climate, the analysis of 1870-control 2 therefore further confirms the two main conclusions concerning the influence of the mean state.

Finally, note that, as in D08, the position of the extrema of variability in SST and SSS in 1870-control is also located in the region of strong horizontal gradients between the two gyres (Figs. 4 and 7). However, in contrast to D08, no local wind forcing anomaly has been found to explain their formation. Instead, the presence of time variable current meanders in the vicinity of the maximum height of the mid-Atlantic ridge located around 40°N, 30°W suggests that this extrema of SST and SSS variability is created by an interaction with the topography.

6. Coupling between surface and MOC variability in the control simulations

In seeking an explanation for the differences in MOC variability between 1870-control and 1990-control, this section investigates the influence on the MOC variability

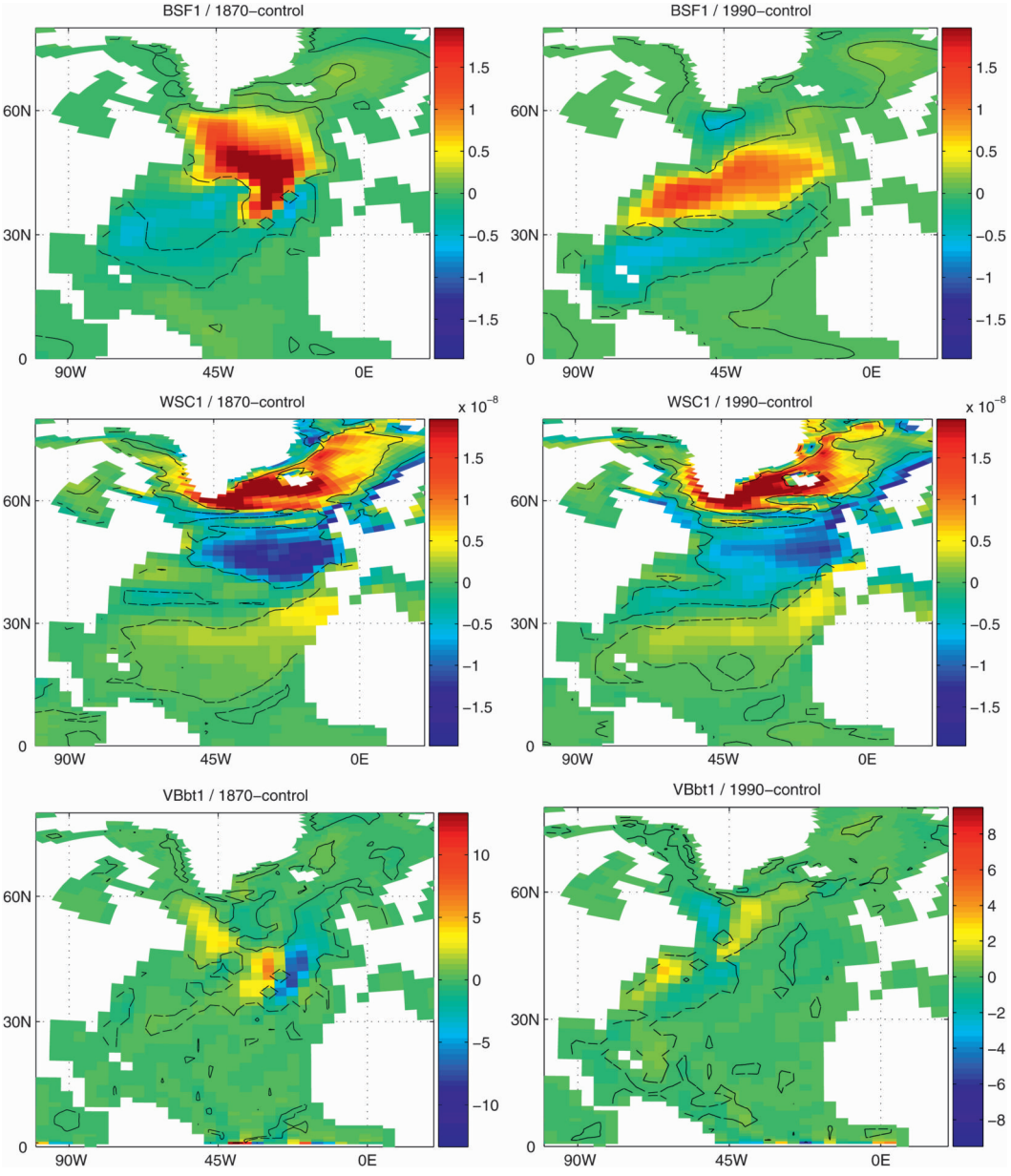

FIG. 9. As in Fig. 7, but for (top) BSF (Sv), (middle) WSC (N m^{-3}), and (bottom) V_{tb} (m^2 s^{-1}).

of the two main differences in surface variability highlighted in the two previous sections: the difference in the amplitude of the SSS and SST variability in the subpolar gyre (resulting from the change of the mean sea ice coverage) and the difference in the variability of the barotropic circulation (resulting from a change of the mean barotropic circulation).

a. SSS and SST relationships with the MOC

In both simulations, a detailed analysis of the different contributions to the heat and freshwater fluxes shows that the variabilities in the total fluxes are dominated by the latent heat flux anomaly and the sea ice melting anomaly, respectively (not shown). Note that evaporation and sea ice melting/formation are the only fluxes that simultaneously impact SST and SSS, but they impact in different ways: an evaporation anomaly or a melting anomaly both damp SST anomalies and create opposite SSS anomalies. From this perspective, it appears that these two contributions to the surface fluxes are deeply involved in positively and negatively coupling SSS and SST anomalies. With more sea ice coverage in the colder experiment 1870-control than 1990-control, the amplitude of the sea ice coverage variability is twice

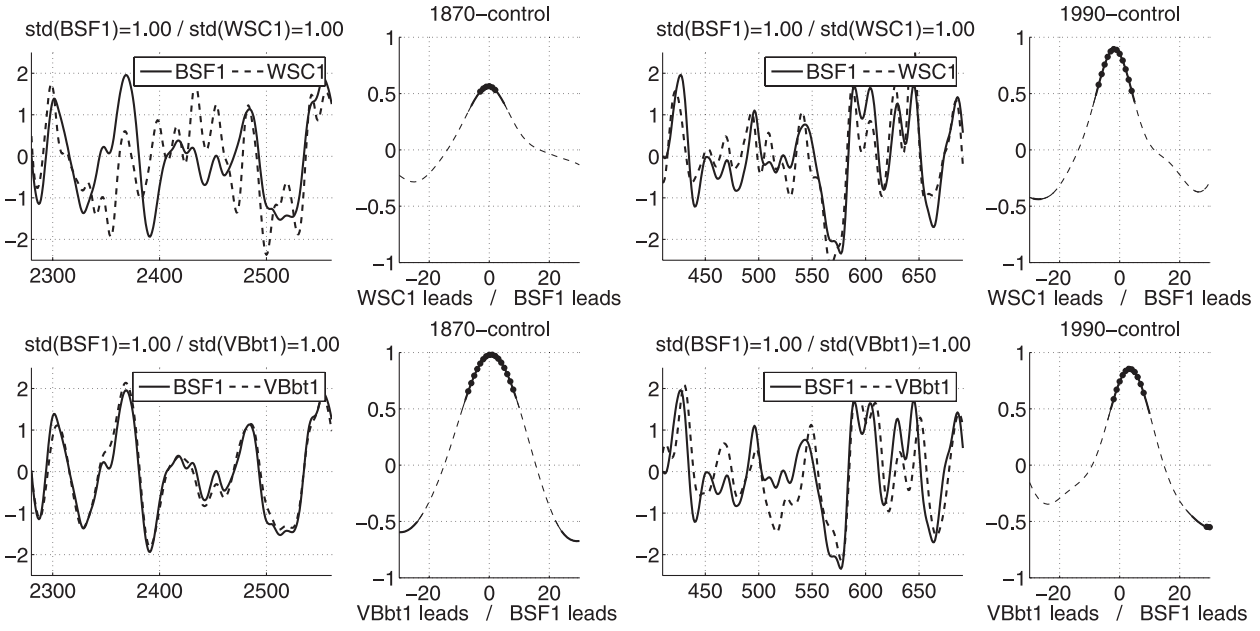

FIG. 10. As in Fig. 8, but (top) between the first EOFs of BSF and WSC and (bottom) between the first EOFs of BSF and V_{tb}. BSF leads for positive lag.

as large (not shown), and a stronger coupling between SST and SSS variability could therefore be expected.

To investigate the cause of the different MOC variability in the two control simulations, an examination of the relation between the MOC index and the surface anomalies in the DWF sites has been performed. The mean winter mixed layer depth (MLD)[2] field indicates three regions of DWF: in the GIN Seas between Spitzbergen and Iceland, south of Iceland along the East Greenland Current, and south of Greenland in the Labrador Sea basin. Time-lag correlations are performed between the MOC index and the MLD anomalies averaged over these three DWF sites. No significant correlation is found between the MOC and the GIN Seas DWF site in either simulation, whereas significant correlations (discussed later) are found between the MOC and the East Greenland Current or the Labrador Sea DWF sites. This implies that MOC variability is connected to subpolar gyre surface conditions.

Time-lag correlations are also performed between the MOC index and the SST and SSS anomalies averaged over the East Greenland Current or the Labrador Sea DWF sites. In 1870-control, both sites show that the SST, SSS, and MLD averages lead the MOC index with a correlation coefficient larger than 0.6 (99%) at a lag of approximately 10 yr (Figs. 11, 12, left). In contrast, in 1990-control, the MOC index is led by the three variables with a lag of approximately 10 yr only at the East Greenland Current DWF site (Fig. 11, right), whereas at the Labrador Sea DWF site only the SSS average reveals a statistically significant correlation at lag −10 yr (Fig. 12, right).

In contrast to previous studies, the contributions of the salinity and temperature anomalies to the surface density anomaly are found to be of opposite sign in the DWF sites. However, the amplitude of the salinity contribution to the density anomaly is always found to be larger than the temperature contribution. This is in sharp contrast with D08, where temperature and salinity contributions to the total density in this DWF region are almost equal and in phase.

The density anomalies at the DWF sites are thus driven by variability in the salinity field. However, it is expected that the corresponding temperature anomalies will modulate the sea ice coverage in such a way as to enhance the deep convection mediated by the salinity variations; a positive (negative) salinity anomaly favors stronger (weaker) winter convection, and the associated positive (negative) temperature anomaly reduces (enhances) the sea ice coverage, allowing an increased heat exchange with the atmosphere.

In 1870-control, the time-lag correlations with the MOC index of the three variables—SST, SSS, and MLD—also reveal a second extremum of opposite sign

[2] Average winter values of MLD have been created by averaging temporally over the three winter months (December–February). Anomalies have then been created by applying the same detrending and the same filtering as described in section 2b. MLD is computed internally during the run of the model, and it is based on a maximum buoyancy gradient criterion.

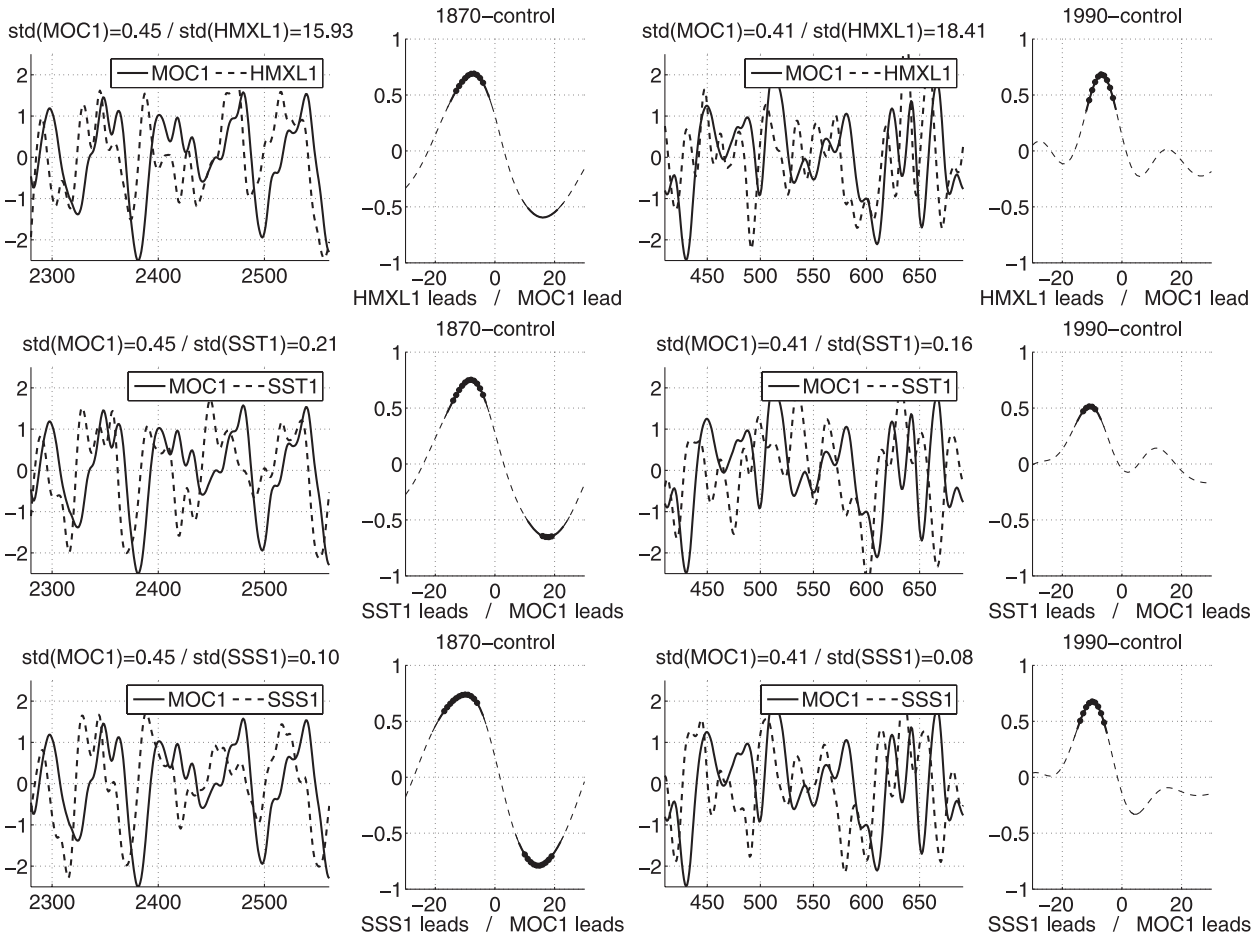

FIG. 11. Time-lag correlations for simulations (left) 1870-control and (right) 1990-control between the MOC index and (top) the average MLD, (middle) the average SST, and (bottom) the average SSS over the East Greenland Current DWF site. Time series are in unit variance, with dimensional std devs given at the top of each plot. Correlation functions of the lag (yr), with statistical significance at the 90% (solid line), 95% (thick solid line), and 99% (large dots) levels. MOC leads with positive lag.

for an opposite lag of approximately 10–15 yr. This second extremum is a direct consequence of the existing quasi-periodic oscillation of the MOC. When the MOC does not oscillate, as in 1990-control (or 1870-control 2), then this second extremum does not exist. This further confirms, not unreasonably, that the MOC is responding to surface conditions in the DWF sites.

Finally, the difference between the two simulations in the Labrador Sea DWF site, together with the difference in mean sea ice coverage, suggests that the coupling between SST and SSS is less strong in 1990-control than in 1870-control. This stronger coupling in colder conditions is further confirmed in 1870-control 2, which displays a SST and SSS variability of similar amplitude to 1870-control but larger than 1990-control.

In conclusion, the MOC variability in the two control simulations is a response delayed by approximately 10 yr to the change of surface conditions at the DWF sites of the subpolar gyre. In 1870-control, the more extensive sea ice coverage increases the coupling and the variability of SSS and SST. This increased coupling is, however, not a sufficient condition for the existence of a quasi-periodic oscillation of the MOC (cf. 1870-control 2).

b. Barotropic circulation and its relationship with the MOC

The relationship between the barotropic circulation and MOC variability in the two simulations is illustrated by the timing of the SPG index (defined as the minimum of the barotropic streamfunction in the North Atlantic) and the MOC index. In Fig. 13, the functional form of the lagged correlations between BSF and MOC are qualitatively similar for both experiments: a negative SPG leads a positive MOC, and a positive MOC is followed by a positive SPG. In other words, an increase of the subpolar gyre transport leads to an increase of the

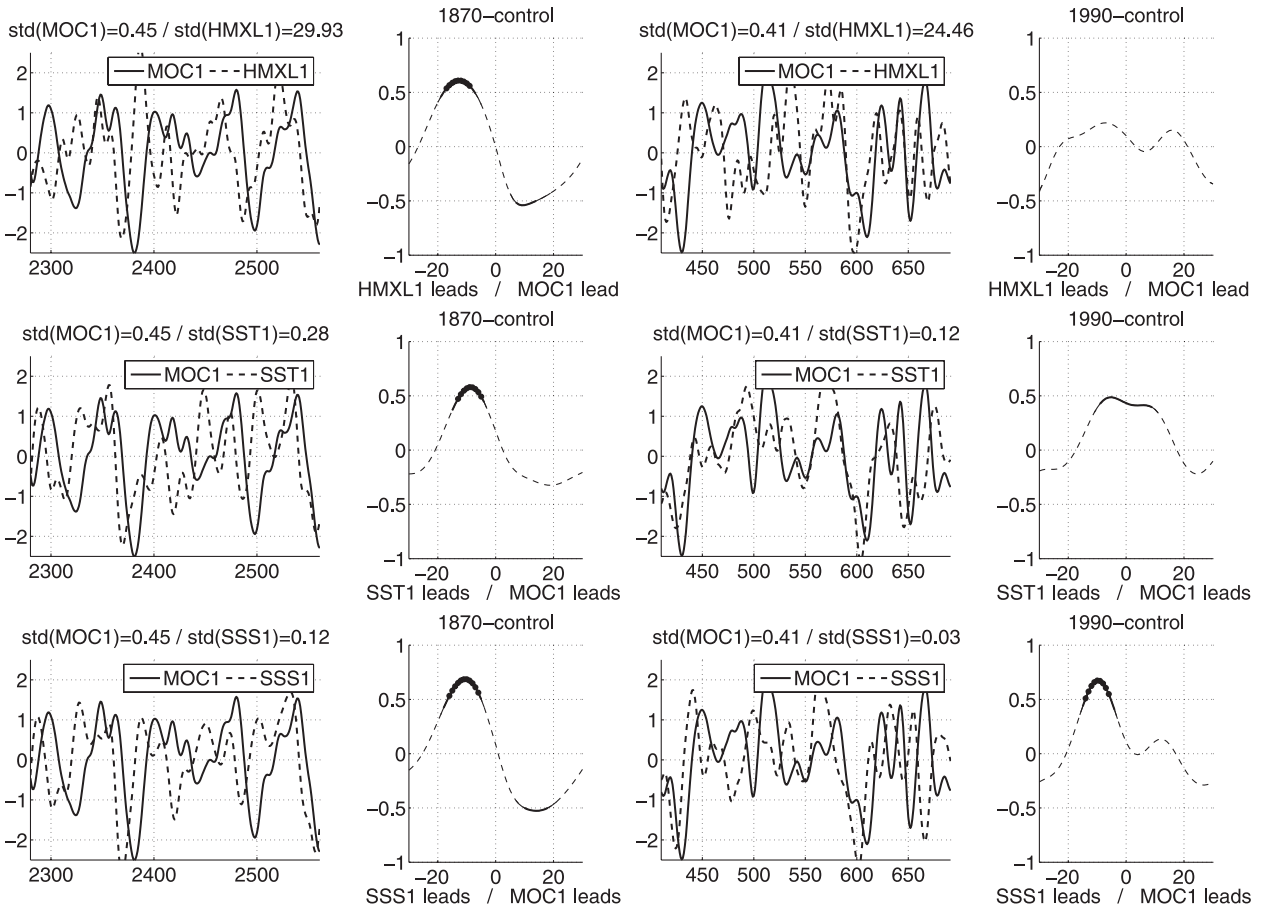

FIG. 12. As in Fig. 11, but in the Labrador Sea DWF site.

thermohaline circulation, and an increase of the thermohaline circulation is followed by a decrease of the subpolar transport. However, the functional forms of Fig. 13 are quantitatively very different in the two experiments: the SPG lead on the MOC is statistically significant at the 99% level only in 1870-control. In contrast, the MOC lead on the SPG is statistically significant at the 99% level in 1990-control and only at the 95% level in 1870-control. However, this second local extrema in 1870-control is probably due to the existence of the quasi-periodic oscillation. In conclusion, it seems therefore that SPG leads the MOC by 12 yr in 1870-control, whereas the MOC leads SPG by 5 yr in 1990-control.

Nevertheless, and in view of the complete set of analyses presented up to this point, we suggest two possibilities. (i) The oscillation can arise as a coupled mechanism between the subpolar gyre and the MOC, where both the weaker subpolar gyre and the more extensive sea ice coverage play a role in maintaining the coupling. (ii) The oscillation of the MOC can arise as a forced response of a free oscillation of the gyre circulation because of its interaction with the bottom bathymetry (favored by the weaker subpolar gyre).

Time-lag regressions of different variables on the SSS anomaly time series of the East Greenland Current DWF site (not shown) reveal that in 1870-control, but not in 1990-control, SSS anomalies tend to grow and decay in the entire subpolar gyre simultaneously with the growth and decay of the barotropic streamfunction anomaly. This indicates that in 1870-control the density anomalies in the DWF sites are likely to be the result of the anomalous advection of the mean salinity and temperature surface gradients rather than originating from the mean advection of localized density anomalies. This anomalous advection may therefore be the link between the barotropic streamfunction variability and the MOC response. In the case of a coupled mechanism between the subpolar gyre and the MOC, the return interaction probably arises from the delayed change of the coupling between the baroclinic and barotropic circulation [term F_{tb} of Eq. (1)] because of the delayed adjustment of the MOC.

In the simulation presented here, this delay has been shown to be on the order of 10 yr, whereas in a control

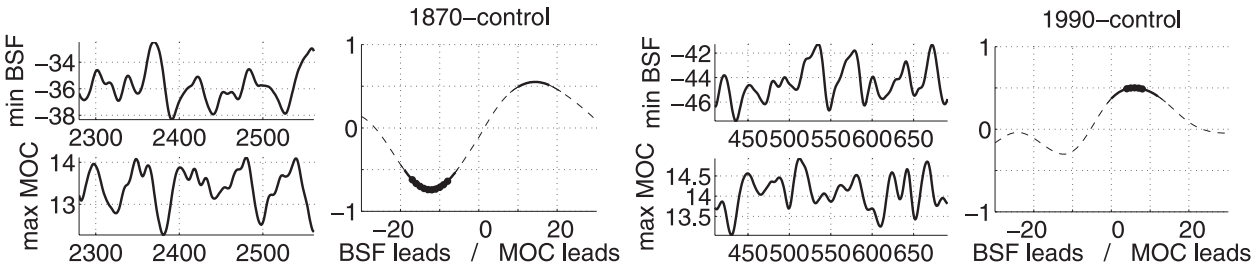

FIG. 13. Simulation (left) 1870-control and (right) 1990-control: time series (Sv) of the MOC and SPG indices and their time-lag correlation, function of the lag in years (statistical significance at the 90% level indicated by solid line, 95% by thick solid line, and 99% by large dots). MOC leads SPG with positive lag.

simulation performed at higher resolution D08 found a delay of only 5 yr. The significant difference in the mean strength of the MOC between the low- and high-resolution simulations (approximately 14 Sv and larger than 20 Sv, respectively) is most likely the explanation for the difference in the delay of the MOC response. This in turn is a likely explanation for the marked increase in the frequency of MOC variability that characterizes the higher-resolution model.

7. Warming simulations

This section investigates the effect of forced warming on the natural multidecadal variability of the North Atlantic. An analysis of the warming experiments (see section 2a and Table 1) is compared to the results obtained for the two control simulations, 1870-control and 1990-control. It is based on the mechanistic indicators used in section 6 to characterize MOC variability mechanisms.

A description of the effects of warming on the mean fields can be found in Bryan et al. (2006), who found that a decline in overturning strength is driven by decreasing density of the subpolar North Atlantic because of increasing surface heat fluxes. Because it has been shown in the previous sections of this paper that MOC variability is a response to surface salinity anomalies, a key question is for what degree of warming will the increase of heat fluxes change the driver of MOC variability.

Note that the warming induced in the realistic twentieth-century simulation, 1870–2000, is weaker than the warming in the first 130 yr of the simulation with an increase of 0.5% in CO_2 concentration per year, 1870–0.5% (Fig. 14). The simulation 1870–2000 will therefore be considered to represent the weakest forcing of all the warming simulations.

a. On the response of the MOC to salinity anomalies

As in section 6a, time-lag correlations between the MOC index and averages over DWF sites of surface condition anomalies have been computed for all warming experiments. Figure 15 presents the results for SSS at the East Greenland Current DWF site for all five simulations. In 1870–1.0%, the SSS variability at this DWF site no longer leads the MOC variability; in 1990–1.0%, the weak correlation amplitude of 0.5 at lag −8 yr is not statistically significant at the 99% level. In the three additional simulations, which are characterized by a weaker forced warming, the SSS variability at the East Greenland Current DWF site continues to lead MOC variability by 10 yr or more.

Except in 1870–2000, the simulation with the weakest forced warming, the SSS variability at the other subpolar DWF site (the Labrador Sea) no longer leads the MOC variability (not shown). The different response of the two sites can certainly be explained by the fact that a large sudden freshening occurs in the Labrador Sea after 100 yr or more of integration. This freshening is due to the advection of much fresher surface water from the Arctic. This is reminiscent of the change of SSS variability in the North Pacific, which is described in Part I. The fact that the East Greenland Current DWF site is not affected by it suggests that this freshening comes mainly from the Canadian Archipelago throughflow. As in the North Pacific, after this freshening occurs, the SSS variability of the Labrador Sea DWF site is dominated by much stronger variability.

In conclusion, for strong forced warming, MOC variability ceases to be a delayed response to the salinity anomalies at the DWF sites of the subpolar gyres. At weaker forcing, the surface condition anomalies at the East Greenland Current DWF site continue to lead MOC variability.

b. On the relationship between the MOC and the barotropic circulation

In all of the four simulations with a constant increase of 0.5% or 1% in CO_2 concentration per year, the MOC amplitude is predicted to decrease (Fig. 16), as already found previously in similar experiments performed with the same CCSM3 model at both low and high resolution

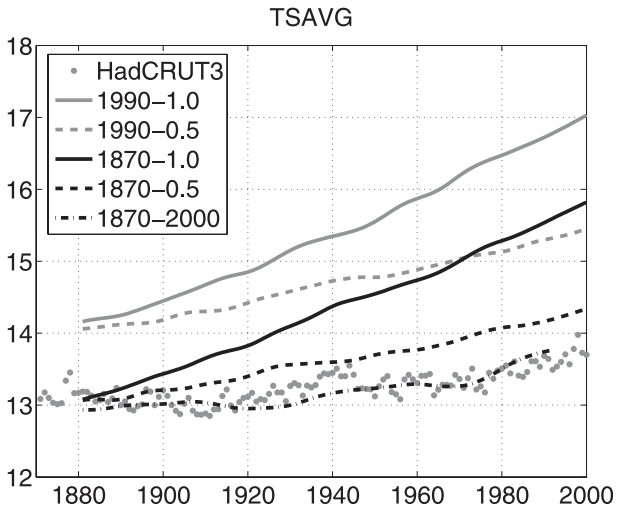

FIG. 14. Average over the entire globe of surface air temperature (°C) in the five warming experiments as a function of time (yr). Averages have been low-pass filtered. Simulations initialized from 1990-control are shown by gray lines (1990–1.0% is solid and 1990–0.5% is dashed). Simulations initialized from 1870-control are shown by black lines (1870–1.0% is solid, 1870–0.5% is dashed, and 1870–2000 is dashed–dotted). Only the first 130 yr period of each simulation is displayed, and the time axis is referenced to the 1870–2000 experiment for convenience. The gray dots correspond to the observed anomalies from the Hadley Centre Climatic Research Unit, version 3 (HadCRUT3) dataset referenced to the 1961–90 period (Brohan et al. 2006), with an offset of 13.4°C to take into account the mean average surface air temperature of simulation 1870–2000 over the same period (1961–90).

(Bryan et al. 2006). In contrast, the MOC amplitude is found to increase in 1870–2000 (Fig. 16). With the highest-resolution version of CCSM3, it was previously demonstrated that the forcing of the twentieth century (the same as employed in the simulation 1870–2000) is not able to significantly impact the MOC amplitude (Meehl et al. 2006). In the simulation 1870–2000, the anomalous increase of the MOC amplitude in 1870–2000 is in fact found to be related to the concomitant change of the subpolar gyre circulation that evolves from a weak state, which is characteristic of 1870-control, to the strong state, which is characteristic of 1990-control (Fig. 16). It can be shown that these two states correspond to two different latitudinal positions of the global North Atlantic maximum of the meridional overturning circulation, at 28°N in 1870-control and at 34°N in 1990-control. The increase of the MOC in 1870–2000 therefore does not result directly from the weak forced warming but from a shift in the mean state induced by the evolving climate.

In the remainder of this section, we will investigate the second key characteristic of the natural variability, which has been shown to be the time-lag correlations between the SPG maximum barotropic transport (denoted as SPG) and the meridional overturning circulation.

In the warming simulations initialized from the 1990-control simulation, the time-lag correlation curves between SPG and MOC do not display the same weak extremum as in the control integration (Figs. 13, 16, right). It can be concluded that the apparent weak coupling between the MOC and the subpolar gyre in 1990-control is further suppressed by the warming in simulations 1990–0.5% and 1990–1.0%.

In the warming simulations initialized from the 1870-control simulation, 1870–2000 and 1870–0.5%, the time-lag correlation curves between SPG and MOC (Fig. 16, left) reveal extrema of correlation values similar to 1870-control (Fig. 13, left), with a strong amplitude maxima larger than 0.7 (99%) when the SPG leads the MOC by approximately 10–15 yr and a secondary extremum when the MOC leads the SPG by approximately 10 yr. Although in 1870–0.5% the second extrema is not statistically significant, those two curves are reminiscent of the results of the simulation 1870-control. For the warming simulation initialized from the 1870-control simulation with the strongest forced warming (1870–1.0%), the time-lag correlation curves between SPG and MOC (Fig. 16, left) display one maximum of magnitude 0.6 (99%) when the MOC index leads by 8 yr. This differs from the results for the simulation 1870-control.

It may be concluded that the strong coupling between the horizontal and overturning circulations in the North Atlantic in the statistical equilibrium run 1870-control is therefore preserved in the warming scenarios, but only if the warming is not overly strong.

8. Discussion

Based on multicentury integrations performed using the low-resolution version of CCSM3, meridional overturning circulation (MOC) variability has been characterized in different control simulations and further investigated in a range of global warming scenarios.

It was first shown that MOC variability is dependent on the control simulation, and two hypotheses have been suggested to explain the well-defined 60-yr periodicity of the MOC found in part of the preindustrial simulation: either the existence of a coupling mechanism between the subpolar gyre and the MOC (where both the weaker subpolar gyre and the more extensive sea ice coverage play a role in maintaining this coupling) or the existence of a free oscillation of the gyre circulation resulting from its interaction with the bottom bathymetry (which is favored by the weaker subpolar gyre and creates periodic SSS and SST anomalies). Note, however, that the quasi-periodic oscillation along with the weaker gyre was only

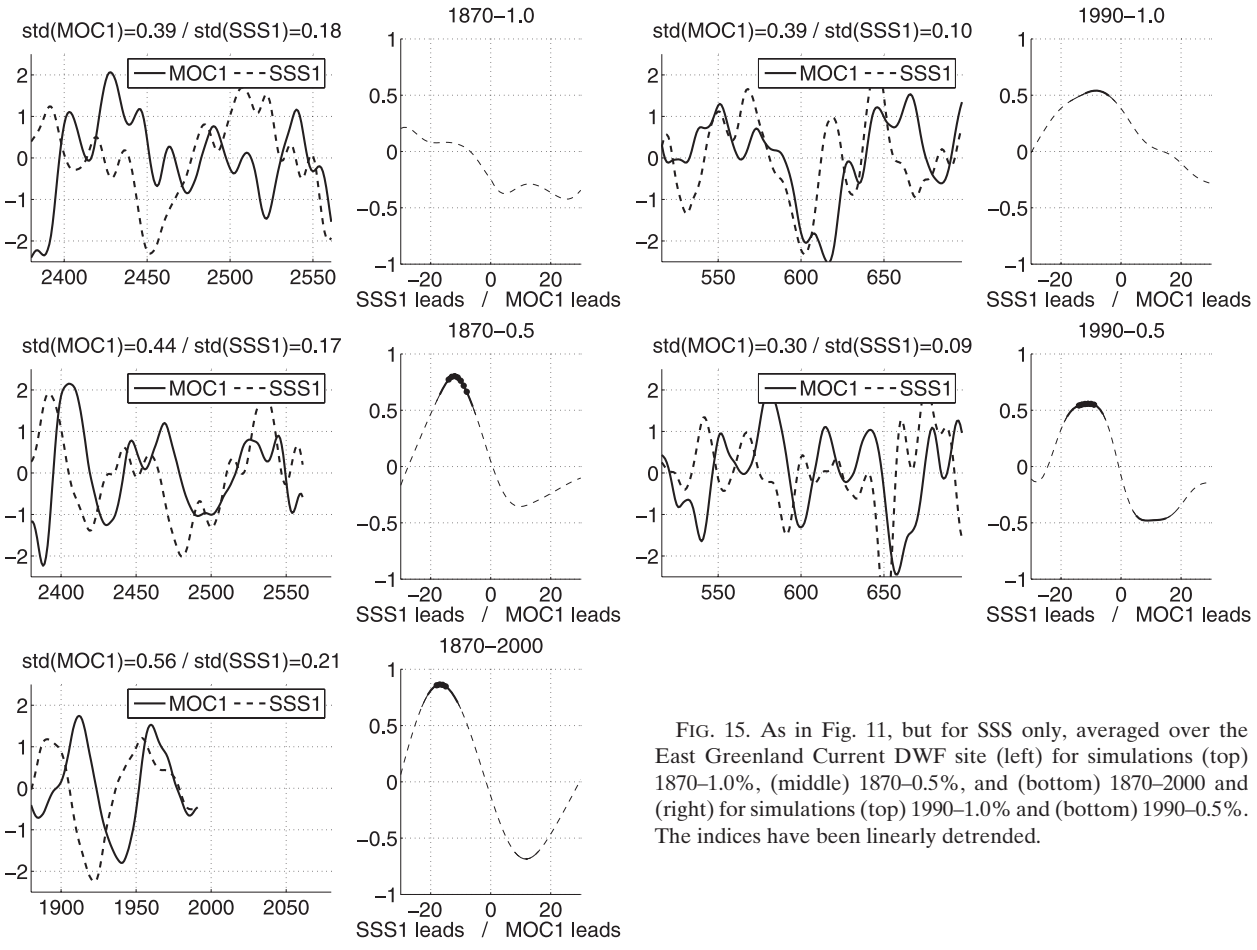

FIG. 15. As in Fig. 11, but for SSS only, averaged over the East Greenland Current DWF site (left) for simulations (top) 1870–1.0%, (middle) 1870–0.5%, and (bottom) 1870–2000 and (right) for simulations (top) 1990–1.0% and (bottom) 1990–0.5%. The indices have been linearly detrended.

present as a transient for 300 yr in the 1870 experiment; therefore, it is not possible to rule out the possibility that the multidecadal fluctuation has active and inactive periods, depending on the mean gyre circulation, which can be stable for centuries at a time. This is one of the several interesting implications of the results of this paper.

In all control simulations, MOC variability has been demonstrated to be a 10-yr delayed response to synchronous temperature and salinity anomalies in the deep water formation sites located in the subpolar gyre. Under sufficiently strong warming (i.e., 1.0% of CO_2 concentration increase per year), this response is suppressed, as is the strong coupling between the subpolar gyre and MOC variability (if it exists in the corresponding control simulation). This suggests, first, that the 10-yr delay of the MOC response to a change of the surface conditions is a necessary condition for the existence of the 60-yr cycle described in the preindustrial control simulation. However, this also demonstrates that the 10-yr delay is not a sufficient condition for the existence of the cycle, because this cycle is absent from the present-day control simulation.

As advocated in D08, the relation between the MOC and sea surface conditions has been illustrated here for the deep water formation sites, because no statistically significant time-lag correlations have been found between basin-wide averages of SSS or SST and the MOC index. Moreover, in contrast to the apparently prevalent idea concerning the relation between the MOC and SST variabilities [i.e., MOC variability modulates the northward heat transport (Bjerknes 1964) and therefore modulates the SST at the deep water formation sites], in our analysis, warmer (colder) SSTs lead a MOC maximum (minimum). In fact, the density anomaly at the deep water formation sites is consistently salinity driven in our simulations, with saltier (fresher) SSS leading a MOC maximum (minimum). If the SST plays a role in the mechanism underlying MOC variability, it could be either in allowing salinity anomalies to be advected by the subpolar gyre by partially compensating the density anomaly or in modulating the sea ice coverage synchronously with the density anomaly.

The effect of increased sea ice coverage in the colder simulation has been shown to be responsible for the

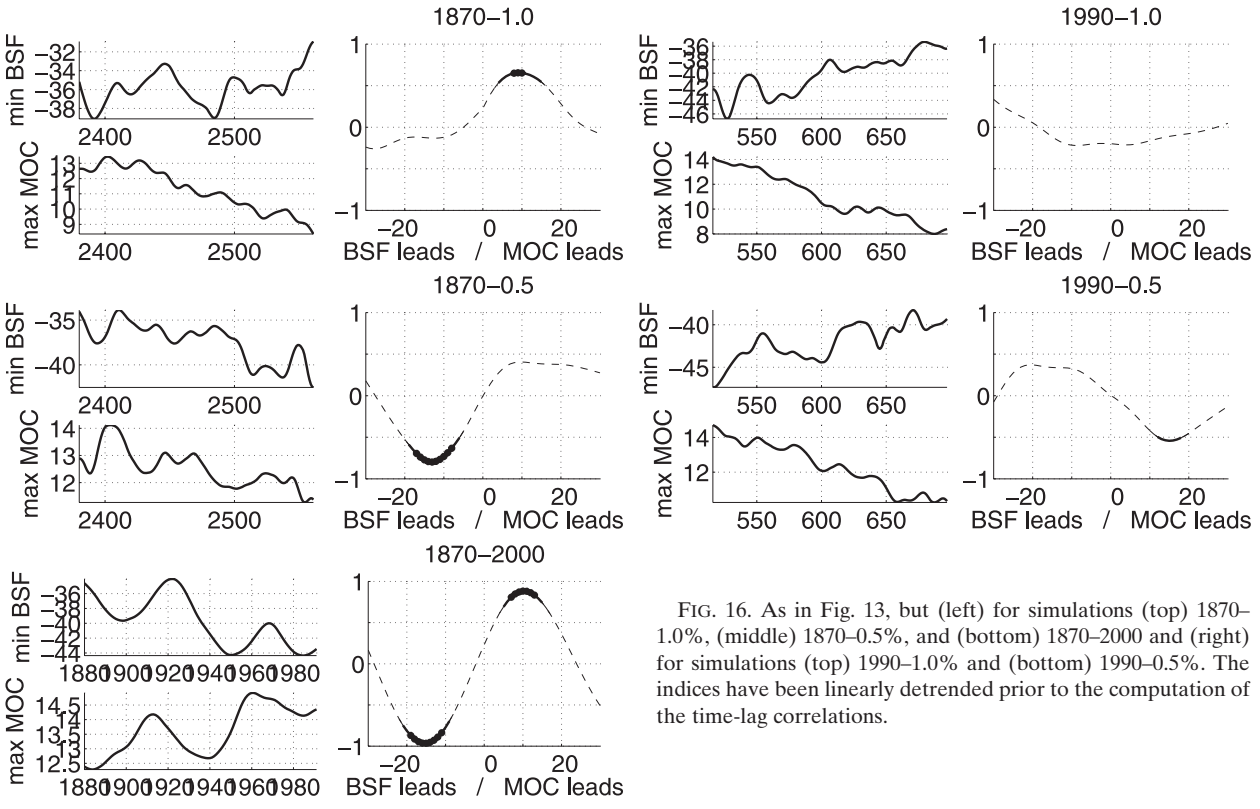

FIG. 16. As in Fig. 13, but (left) for simulations (top) 1870–1.0%, (middle) 1870–0.5%, and (bottom) 1870–2000 and (right) for simulations (top) 1990–1.0% and (bottom) 1990–0.5%. The indices have been linearly detrended prior to the computation of the time-lag correlations.

increase of SSS and SST variability in the subpolar gyre. However, no increase of the MOC variability at interannual or multidecadal time scales has been revealed, because standard deviations of the MOC index are 0.4 Sv after low-pass filtering and 0.9 Sv without for all control simulations. Moreover, the increase of sea ice coverage has been shown to not be a sufficient condition to explain the well-defined periodicity of the modeled MOC.

In warming experiments, it has been previously demonstrated that the amplitude of the reduction of the MOC is a function of mean climate from which warming ensues. As described by Weaver et al. (2007), the results basically separate into two cases: cold climate with extensive sea ice, which prevents deep water formation in the Labrador Sea, and warm climate with reduced sea ice, which allows deep water formation in the Labrador Sea. Not only is the influence of the mean state on the average reduction of the MOC retrieved here (one can compare the MOC decrease in Fig. 16 for a pair of simulations with the same CO_2 concentration increase), but the mean state also has an effect on the variability of the MOC and more generally on the North Atlantic multidecadal variability. This influence is apparently not captured in the model of intermediate complexity employed by Weaver et al. (2007), which does not seem to display any multidecadal variability of the MOC. Because of the simplicity of the atmospheric component of their model, this raises the question of the role of the atmosphere in the multidecadal variability of the MOC.

In both control simulations, the leading EOFs of both SST and wind stress curl have similar spatial patterns: tripole and dipole, respectively (Figs. 7 and 9). These structures are reminiscent of the classical North Atlantic Oscillation (NAO) pattern. Therefore, as already suggested by many authors (Delworth et al. 1993; Dai et al. 2005; Dong and Sutton 2005; D08), the NAO could also play a role in MOC variability by, for instance, modulating sea ice melting/formation and evaporation, which dominates the variability of the heat and freshwater fluxes in the North Atlantic in our simulation. However, in the case of the quasi-periodic MOC variability in the preindustrial control simulation, the origin of the 60-yr period has been related to the variability of the barotropic circulation, which has been demonstrated to involve an interaction with the bottom bathymetry and not to be a direct response to the wind forcing, therefore excluding the NAO as the leading mechanism driving the MOC variability in this simulation.

Acknowledgments. The work reported in this paper is a contribution to the Polar Climate Stability Network, which is funded by the Canadian Foundation for

Climate and Atmospheric Science and a consortium of Canadian universities. Additional support was provided by NSERC Grant 9627.

REFERENCES

Bjerknes, J., 1964: Atlantic air-sea interaction. *Adv. Geophys.,* **10,** 1–82.

Bretherton, C. S., M. Widmann, V. P. Dymnikov, J. M. Wallace, and I. Bladé, 1999: The effective number of spatial degrees of freedom of a time-varying field. *J. Climate,* **12,** 1990–2009.

Brohan, P., J. J. Kennedy, I. Harris, S. F. B. Tett, and P. D. Jones, 2006: Uncertainty estimates in regional and global observed temperature changes: A new data set from 1850. *J. Geophys. Res.,* **111,** D12106, doi:10.1029/2005JD006548.

Bryan, F. O., G. Danabasoglu, N. Nakashiki, Y. Yoshida, D. H. Kim, J. Tsutsui, and S. C. Doney, 2006: Response of North Atlantic thermohaline circulation and ventilation to increasing carbon dioxide in CCSM3. *J. Climate,* **19,** 2382–2397.

Collins, W. D., and Coauthors, 2006: The Community Climate System Model version 3 (CCSM3). *J. Climate,* **19,** 2122–2143.

Dai, A., A. Hu, G. A. Meehl, W. M. Washington, and W. G. Strand, 2005: Atlantic thermohaline circulation in a coupled general circulation model: Unforced variations versus forced changes. *J. Climate,* **18,** 3270–3293.

Danabasoglu, G., 2008: On multidecadal variability of the Atlantic meridional overturning circulation in the Community Climate System Model version 3 (CCSM3). *J. Climate,* **21,** 5524–5544.

Delworth, T. L., and R. J. Greatbatch, 2000: Multidecadal thermohaline circulation variability driven by atmospheric surface flux forcing. *J. Climate,* **13,** 1481–1495.

——, and M. E. Mann, 2000: Observed and simulated multidecadal variability in the northern hemisphere. *Climate Dyn.,* **16,** 661–676.

——, S. Manabe, and R. J. Stouffer, 1993: Interdecadal variations of the thermohaline circulation in a coupled ocean–atmosphere model. *J. Climate,* **6,** 1993–2011.

——, ——, and ——, 1997: Multidecadal climate variability in the Greenland Sea and surrounding regions: A coupled model simulation. *Geophys. Res. Lett.,* **24,** 257–260.

Deser, C., and M. L. Blackmon, 1993: Surface climate variations over the North Atlantic Ocean during winter: 1900–1989. *J. Climate,* **6,** 1743–1753.

Dong, B., and R. T. Sutton, 2005: Mechanism of interdecadal thermohaline circulation variability in a coupled ocean–atmosphere GCM. *J. Climate,* **18,** 1117–1135.

——, ——, and A. A. Scaife, 2006: Multidecadal modulation of El Niño–Southern Oscillation (ENSO) variance by Atlantic Ocean sea surface temperatures. *Geophys. Res. Lett.,* **33,** L08705, doi:10.1029/2006GL025766.

d'Orgeville, M., and W. R. Peltier, 2007: On the Pacific Decadal Oscillation and the Atlantic Multidecadal Oscillation: Might they be related? *Geophys. Res. Lett.,* **34,** L23705, doi:10.1029/2007GL031584.

——, and ——, 2009: Implications of both statistical equilibrium and global warming simulations with CCSM3. Part I: On the decadal variability in the North Pacific basin. *J. Climate,* **22,** 5277–5297.

Enfield, D. B., A. M. Mestas-Nuñez, and P. J. Trimble, 2001: The Atlantic multidecadal oscillation and its relation to rainfall and river flows in the continental U.S. *Geophys. Res. Lett.,* **28,** 2077–2080.

Goldenberg, S. B., C. Landsea, A. M. Mestas-Nuñez, and W. M. Gray, 2001: The recent increase in Atlantic hurricane activity. *Science,* **293,** 474–479.

Gray, S. T., L. J. Graumlich, J. L. Betancourt, and G. T. Pederson, 2004: A tree-ring based reconstruction of the Atlantic Multidecadal Oscillation since 1567 A.D. *Geophys. Res. Lett.,* **31,** L12205, doi:10.1029/2004GL019932.

Greatbatch, R. J., A. F. Fanning, A. D. Goulding, and S. Levitus, 1991: A diagnosis of interpentadal circulation changes in the North Atlantic. *J. Geophys. Res.,* **96,** 22 009–22 023.

Knight, J. R., R. J. Allan, C. K. Folland, M. Vellinga, and M. E. Mann, 2005: A signature of persistent natural thermohaline circulation cycles in observed climate. *Geophys. Res. Lett.,* **32,** L20708, doi:10.1029/2005GL024233.

Large, W. G., and G. Danabasoglu, 2006: Attribution and impacts of upper-ocean biases in CCSM3. *J. Climate,* **19,** 2325–2346.

Mann, M., and J. Lees, 1996: Robust estimation of background noise and signal detection in climatic time series. *Climatic Change,* **33,** 409–445.

McCabe, G. J., M. A. Palecki, and J. L. Betancourt, 2004: Pacific and Atlantic Ocean influences on multidecadal drought frequency in the United States. *Proc. Natl. Acad. Sci. USA,* **101,** 4136–4141.

Meehl, G. A., and Coauthors, 2006: Climate change projections for the twenty-first century and climate change commitment in the CCSM3. *J. Climate,* **19,** 2597–2616.

Mellor, G. L., C. R. Mechoso, and E. Keto, 1982: A diagnostic calculation of the general circulation of the Atlantic Ocean. *Deep-Sea Res.,* **29A,** 1171–1192.

Molinari, R. L., and A. M. Mestas-Nuñez, 2003: North Atlantic decadal variability and the formation of tropical storms and hurricanes. *Geophys. Res. Lett.,* **30,** 1541, doi:10.1029/2002GL016462.

Rayner, N. A., D. E. Parker, E. B. Horton, C. K. Folland, L. V. Alexander, D. P. Rowell, E. C. Kent, and A. Kaplan, 2003: Global analyses of sea surface temperature, sea ice, and night marine air temperature since the late nineteenth century. *J. Geophys. Res.,* **108,** 4407, doi:10.1029/2002JD002670.

Rogers, J. C., and J. S. M. Coleman, 2003: Interactions between the Atlantic Multidecadal Oscillation, El Niño/La Niña, and the PNA in winter Mississippi Valley stream flow. *Geophys. Res. Lett.,* **30,** 1518, doi:10.1029/2003GL017216.

Rowell, D. P., C. K. Folland, K. Maskell, and M. N. Ward, 1995: Variability of summer rainfall over tropical North Africa (1906–92): Observations and modeling. *Quart. J. Roy. Meteor. Soc.,* **121,** 669–704.

Salmon, R., 1998: *Lectures on Geophysical Fluid Dynamics*. Oxford University Press, 378 pp.

Saravanan, R., and J. C. McWilliams, 1997: Stochasticity and spatial resonance in interdecadal climate fluctuations. *J. Climate,* **10,** 2299–2320.

Schlesinger, M. E., and N. Ramankutty, 1994: An oscillation in the global climate system of period 65–70 years. *Nature,* **367,** 723–726.

Smith, T. M., and R. W. Reynolds, 2004: Improved extended reconstruction of SST (1854–1997). *J. Climate,* **17,** 2466–2477.

Sutton, R. T., and D. L. R. Hodson, 2005: Atlantic Ocean forcing of North American and European summer climate. *Science,* **309,** 115–118, doi:10.1126/science.1109496.

Timmermann, A., M. Latif, R. Voss, and A. Grötzner, 1998: Northern Hemispheric interdecadal variability: A coupled air–sea mode. *J. Climate,* **11,** 1906–1931.

Trenberth, K. E., and D. J. Shea, 2006: Atlantic hurricanes and natural variability in 2005. *Geophys. Res. Lett.,* **33,** L12704, doi:10.1029/2006GL026894.

Weaver, A. E., and E. S. Sarachik, 1991: The role of mixed boundary conditions in numerical models of the ocean's climate. *J. Phys. Oceanogr.,* **21,** 1470–1493.

Weaver, A. J., and S. Valcke, 1998: On the variability of the thermohaline circulation in the GFDL coupled model. *J. Climate,* **11,** 759–767.

——, M. Eby, M. Kienast, and O. A. Saenko, 2007: Response of the Atlantic meridional overturning circulation to increasing atmospheric CO_2: Sensitivity to mean climate state. *Geophys. Res. Lett.,* **34,** L05708, doi:10.1029/2006GL028756.

Winton, M., and E. S. Sarachik, 1993: Thermohaline oscillations induced by strong steady salinity forcing of ocean general circulation models. *J. Phys. Oceanogr.,* **23,** 1389–1410.

Yeager, S. G., C. A. Shields, W. G. Large, and J. J. Hack, 2006: The low-resolution CCSM3. *J. Climate,* **19,** 2545–2566.

Zhang, R., and G. K. Vallis, 2007: The role of bottom vortex stretching on the path of the North Atlantic western boundary current and on the northern recirculation gyre. *J. Phys. Oceanogr.,* **37,** 2053–2080.

——, T. L. Delworth, and I. M. Held, 2007: Can the Atlantic Ocean drive the observed multidecadal variability in Northern Hemisphere mean temperature? *Geophys. Res. Lett.,* **34,** L02709, doi:10.1029/2006GL028683.